Electronic Supplementary Material (ESI) for Energy & Environmental Science.
This journal is © The Royal Society of Chemistry 2024

# Supporting Information

## Heteroanion induced structural asymmetricity centered on Ru sites switches the rate-determining step of acid water oxidation

Ding Chen[1], Hongyu Zhao[1], Ruohan Yu[2], Kesong Yu[1], Jiawei Zhu[1], Jixiang Jiao[1], Xueqin Mu[1], Jun Yu[1], Jinsong Wu[2], Shichun Mu[* 1]

[1]*State Key Laboratory of Advanced Technology for Materials Synthesis and Processing, Wuhan University of Technology, Wuhan 430070, China.*

[2]*NRC (Nanostructure Research Centre), Wuhan University of Technology, Wuhan 430070, China.*

** Corresponding author E-mail: msc@whut.edu.cn*

## 1. Experimental Details

### 1.1 Materials and Reagents

Ruthenium (IV) oxide monohydrate ($RuO_2 \cdot H_2O$) was purchased from Wokai Reagents Ltd. Selenium powder (Se) and sulfur powder (S) were obtained from Aladdin Reagents Ltd. Anhydrous lithium chloride (LiCl) and potassium chloride (KCl), sulfuric acid ($H_2SO_4$) and isopropyl alcohol were purchased from Sinopharm Chemical Reagent Co., Ltd. Commercial $RuO_2$, Pt/C (20 wt%) and Nafion (5 wt%) were obtained from Sigma-Aldrich. All the reagents are analytical grade and used without further treatment. Deionized (DI) water was employed as solvent.

### 1.2 Material Syntheses

Target catalyst $Ru_2(S_3Se)$ was obtained via one-pot molten salt-assisted route. First, 140 mg $RuO_2 \cdot H_2O$, 288 mg S powder and 237 mg Se powder were mixed with 2.5 g eutectic salt KCl-LiCl ($n_{KCl}$: $n_{LiCl}$=4.1:5.9) and ground under exclusion of water and oxygen into a fine powder. Then mixture was added into a corundum boat and heated for 4 hours at 800 °C under inert atmosphere. After cooled to room temperature, the reaction product was collected and washed with deionized water and dilute sulfuric acid to remove the residual impurities. Finally, after vacuum dried at 60 °C overnight, the $Ru_2(S_3Se)$ was obtained. The pristine $RuS_2$ was obtained by the molten salt-assisted strategy without Se powder, and the pristine $RuSe_2$ was obtained by the molten salt-assisted strategy without S powder.

### 1.3 Material Characterization

X-ray diffraction (XRD) patterns were collected on a Rigaku X-ray diffractometer equipped with a Cu $K\alpha$ radiation source to obtain the crystalline structure of all samples. X-ray photoelectron spectroscopy (XPS) and synchrotron radiation X-ray absorption spectroscopy (XAS) were carried out to reveal the electronic structure and valence bond structure. The morphology and structure were characterized by double spherical aberration-corrected scanning transmission electron microscope (AC-STEM, Titan Cubed Themis G2 300). Inductively coupled plasma (ICP) was carried on NexION 300 (PerkinElmer) for the leaching measurements. Raman spectra were obtained at a Renishaw Raman Imaging Microscope System (inVia-Reflex) equipped with a CCD detector. Excitation radiation at 532 nm was used. Fourier transform infrared spectroscopy (FTIR) spectrum for powder was collected on a Nicolet 6700 Fourier Transform Infrared Spectrometer.

**1.4 Electrochemical Measurements**

All electrochemical measurements were performed in a conventional three-electrode system at room temperature using a CHI 660E electrochemical analyzer (CHI Instruments, Shanghai, China). The acidic (0.5 M $H_2SO_4$) electrochemical measurements were performed using a saturated calomel electrode (SCE) as the reference electrode, a graphite plate as the counter electrode, and a glassy carbon electrode (GCE) with a diameter of 3 mm as the working electrode. The catalyst ink was prepared by dispersing 7 mg as-prepared sample and 3 mg conductive XC-72 powder into a mixture (700 μL isopropyl alcohol, 300 μL water and 20 μL 5% Nafion solution) and ultrasonic dispersion for 30 min. For comparison, 5 mg commercial $RuO_2$ was evenly dispersed into the same mixture. The catalyst inks applied on GCE are all

6 μL. Polarization data were obtained at a scan rate of 5 mV $s^{-1}$. All polarization curves were iR-corrected. The electrochemical impedance spectroscopy (EIS) was conducted at the corresponding potentials of 10 mA $cm^{-2}$ from LSV curves, with the frequency range of 0.01 Hz to 100 kHz with AC amplitude of 10 mV. The electrochemical double layer capacitance ($C_{dl}$) was determined with typical cyclic voltammetry (CV) measurements at various scan rates (20, 40, 60, 80 and 100 mV $s^{-1}$) in nonreactive region. ECSAs of sample was obtained from the measured $C_{dl}$. Notably, the charging of double layer is originated from the non-Faradaic currents which has a linear relationship with the active surface area; the 1 $cm^2$ of flat surface area has a specific capacitance which is equal to $C_{dl}$ value of 60 μF $cm^{-2}$. Therefore, the $C_{dl}$ is directly related with the ECSA as: ECSA = $C_{dl}$ of catalyst (mF $cm^{-2}$) / 0.06 (mF $cm^{-2}$). For the mass activity calculations, the current density at a certain potential in LSV polarization curves was normalized with total mass of Ru loaded on GCE electrode which was determined from the amount of catalyst ink coating. For the specific activity calculations, the current density at a certain potential in LSV polarization curves was normalized with ECSA value. The durability was evaluated by accelerated degradation measurements and constant current chronopotentiometry.

**1.5 DFT Calculations**

DFT calculations in this work were carried out using the CASTEP program on Materials Studio.[1-2] The exchange-correlation effects were described by the Perdew-Burke-Ernzerhof (PBE) functional within the generalized gradient approximation (GGA) method.[3-4] The core-valence interactions were accounted by the projected augmented wave (PAW) method.[5] The energy cutoff for plane wave expansions was set to 450 eV, and the 3×3×1 Monkhorst-Pack grid k-points were selected to sample the Brillouin zone integration. The vacuum space is adopted 20 Å above the surfaces to avoid periodic interactions. The structural optimization was completed for energy and force convergence set at $1.0\times10^{-5}$ eV and 0.02 eV $Å^{-1}$, respectively.

The OER process is divide into the four fundamental reactions as following:

（1） $H_2O + * = OH* + H^+ + e^-$

（2） $OH* = O* + H^+ + e^-$

（3） $O* + H_2O = OOH* + H^+ + e^-$

（4） $OOH* = O_2 + H^+ + e^-$

OOH*, O* and OH* present the OOH, O and OH moieties on the adsorption site.

The Gibbs Free Energy Variation

The change in Gibbs free energy (△G) of each adsorbed intermediate is calculated based on the computational hydrogen electrode method developed by Nørskov et al.8 At standard condition (T = 298.15 K, pH = 0, and U = 0 V (vs. SHE)), the free energy G is defined as the following equation:

$$\triangle G = \triangle E + \triangle E_{ZPE} - T\triangle S$$

Where △E is the energy change obtained from DFT calculation, $\triangle E_{ZPE}$ is the difference between the adsorbed state and gas, which was calculated by summing vibrational frequency for all model based on the equation: $E_{ZPE} = 1/2\sum h\nu_i$ (T is the temperature (298.15 K) in the above reaction system, and △S represents the difference on the entropies between the adsorbed state and gas phase.

Reference

[1] G. Kresse, J. Hafner, Ab Initiomolecular Dynamics for Liquid Metals, *Phys. Rev. B* 47 (**1993**) 558-561.

[2] G. Kresse, J. Hafner, Ab Initiomolecular-Dynamics Simulation of the Liquid-Metal-Amorphous-Semiconductor Transition in Germanium, *Phys. Rev. B* 49 (**1994**) 14251-14269.

[3] J. P. Perdew, K. Burke, M. Ernzerhof, Generalized Gradient Approximation Made Simple. *Phys. Rev. Lett.* 77 (**1996**) 3865-3868.

[4] G. Kresse, D. Joubert, From Ultrasoft Pseudopotentials to the Projector Augmented-Wave Method. *Phys. Rev. B* 59 (**1999**) 1758-1775.

[5] P. E. Blöchl, Projector Augmented-Wave Method, *Phys. Rev. B* 50 (**1994**) 17953-17979.

## 2. Supplementary Figures and Tables

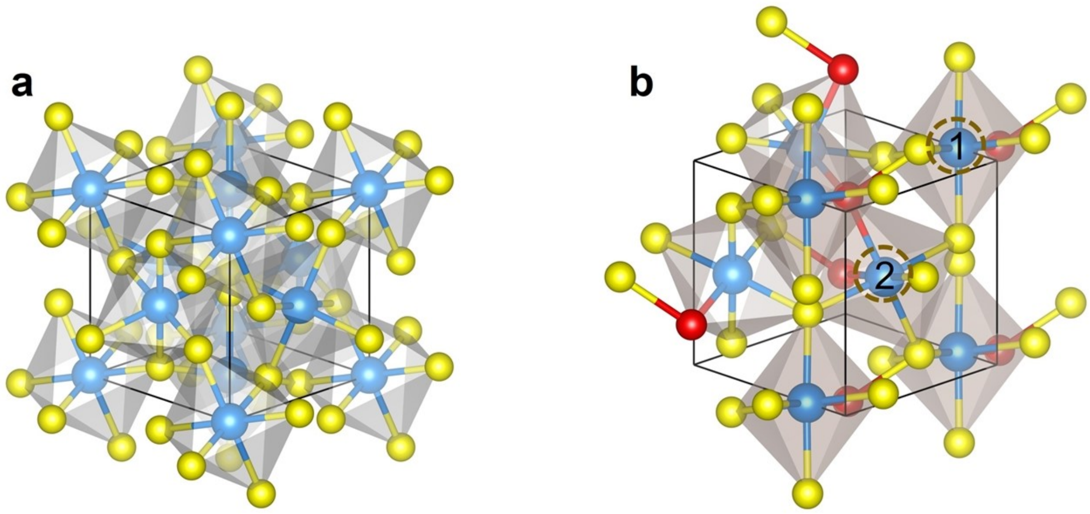


**Figure S1.** The crystal structure of (a) $RuS_2$ and (b) $Ru_2(S_3Se)$.

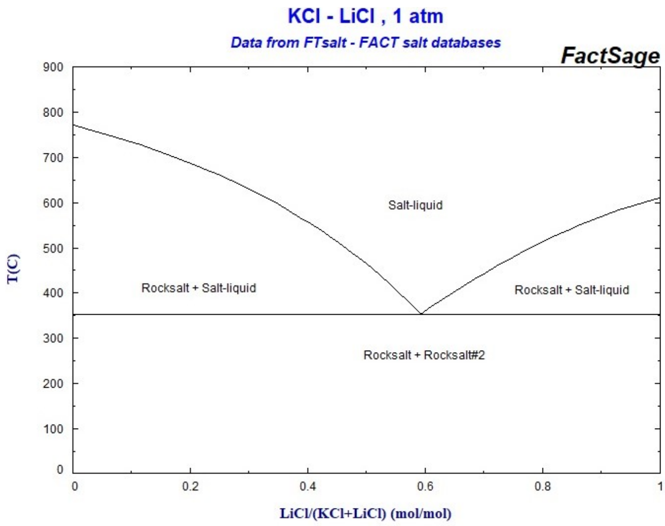


**Figure S2.** The phase diagram of the two-salt system (KCl + LiCl), which coming from the http://www.crct.polymtl.ca/FACT/documentation/ (FTsalt → KCl-LiCl).

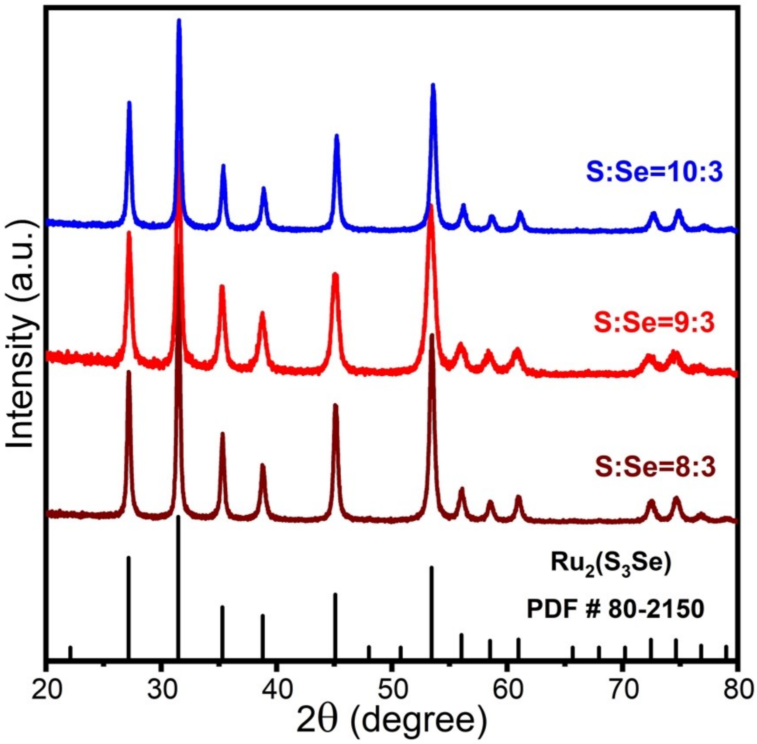


**Figure S3.** XRD patterns of synthesized samples with different S/Se ratio.

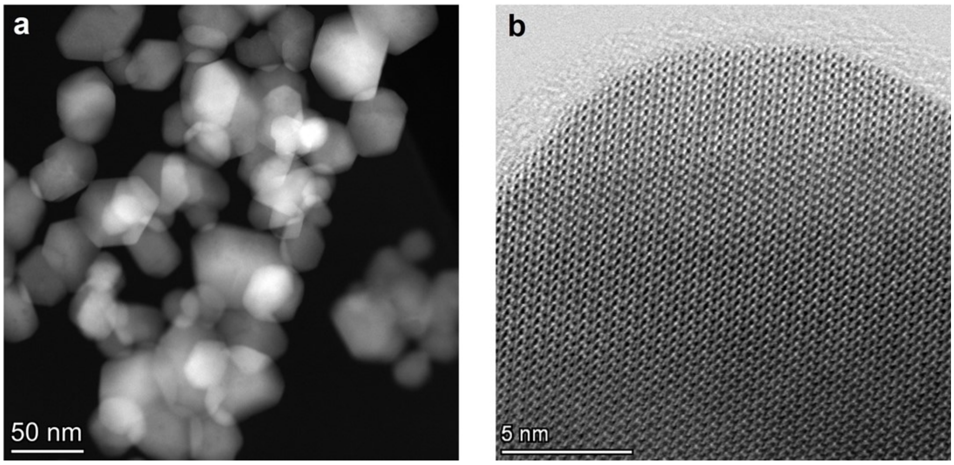


**Figure S4.** Corresponding HAADF and BF-STEM image of figure 1d and figure 1e, respectively.

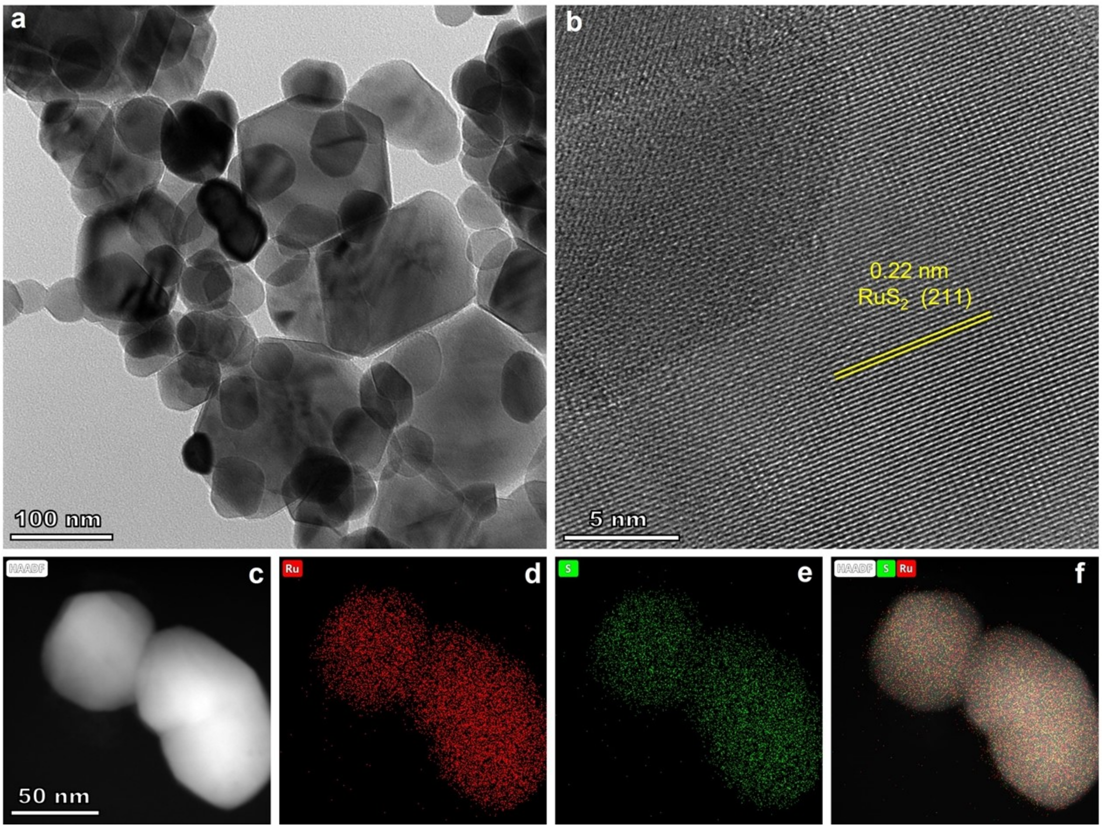


**Figure S5.** STEM images and corresponding EDS elemental maps for Ru, S of $RuS_2$.

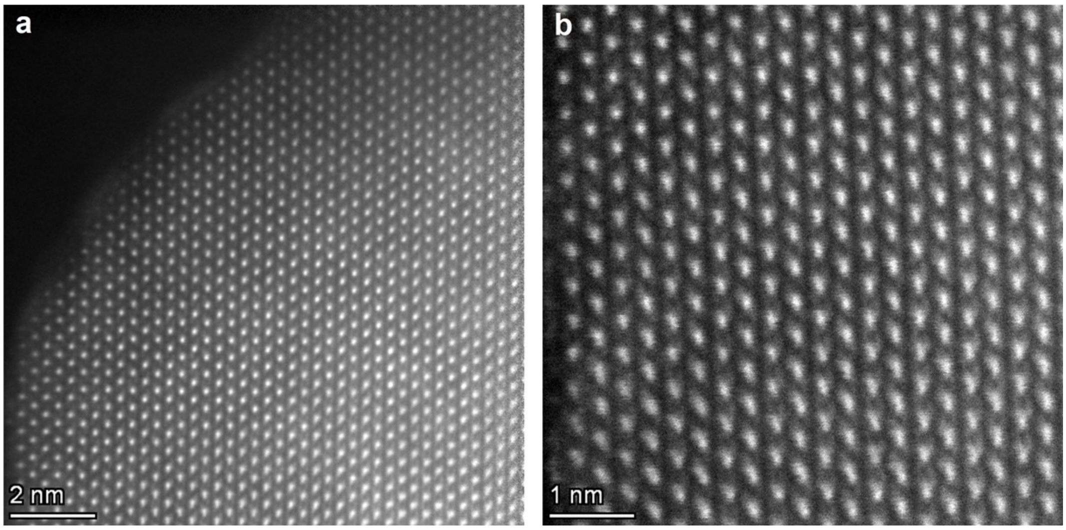


**Figure S6.** Corresponding high-resolution atomic images of $Ru_2(S_3Se)$.

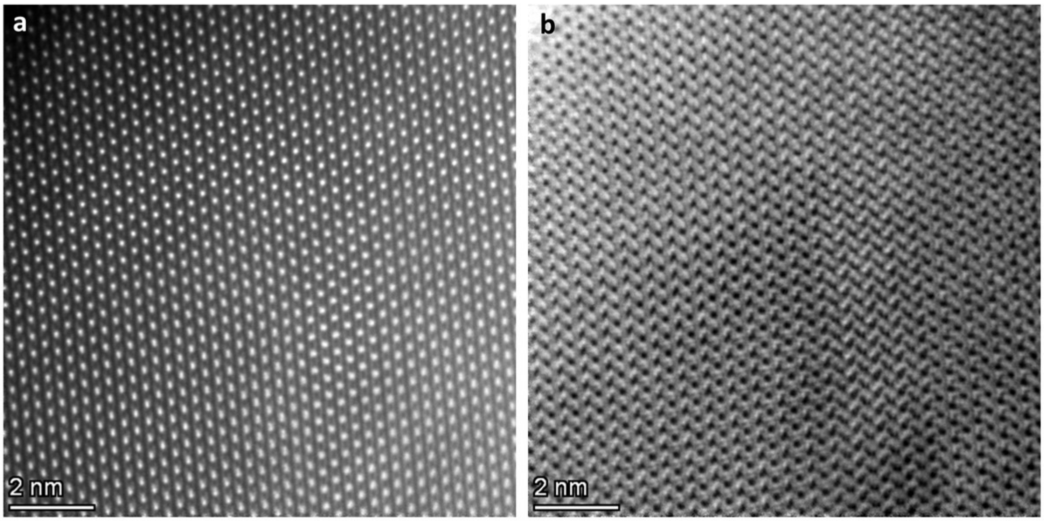


**Figure S7.** (a) HAADF and (b) corresponding BF-STEM images of $Ru_2(S_3Se)$.

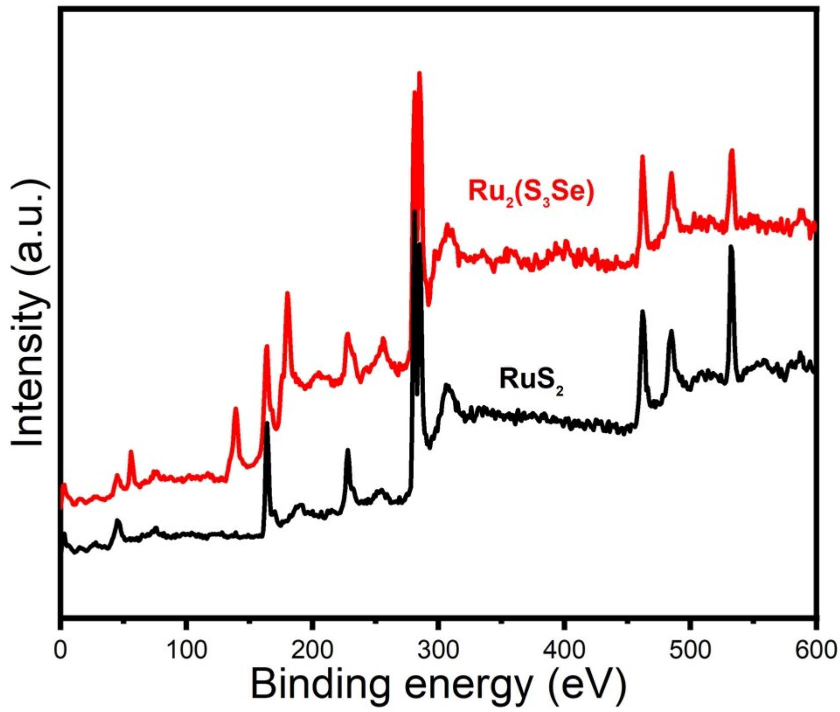


**Figure S8.** XPS survey patterns of $RuS_2$ and $Ru_2(S_3Se)$.

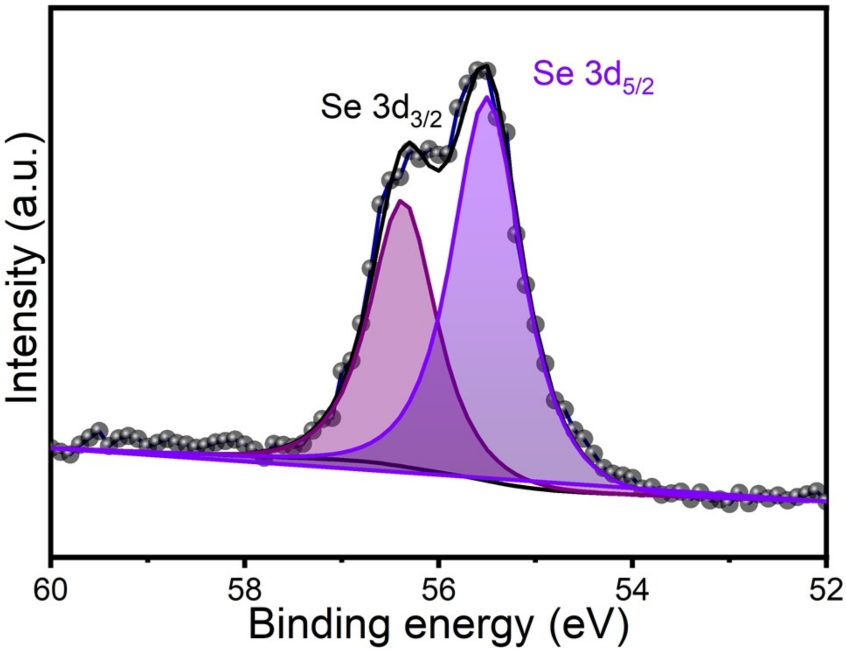


**Figure S9.** Se 3d XPS spectrum of $Ru_2(S_3Se)$.

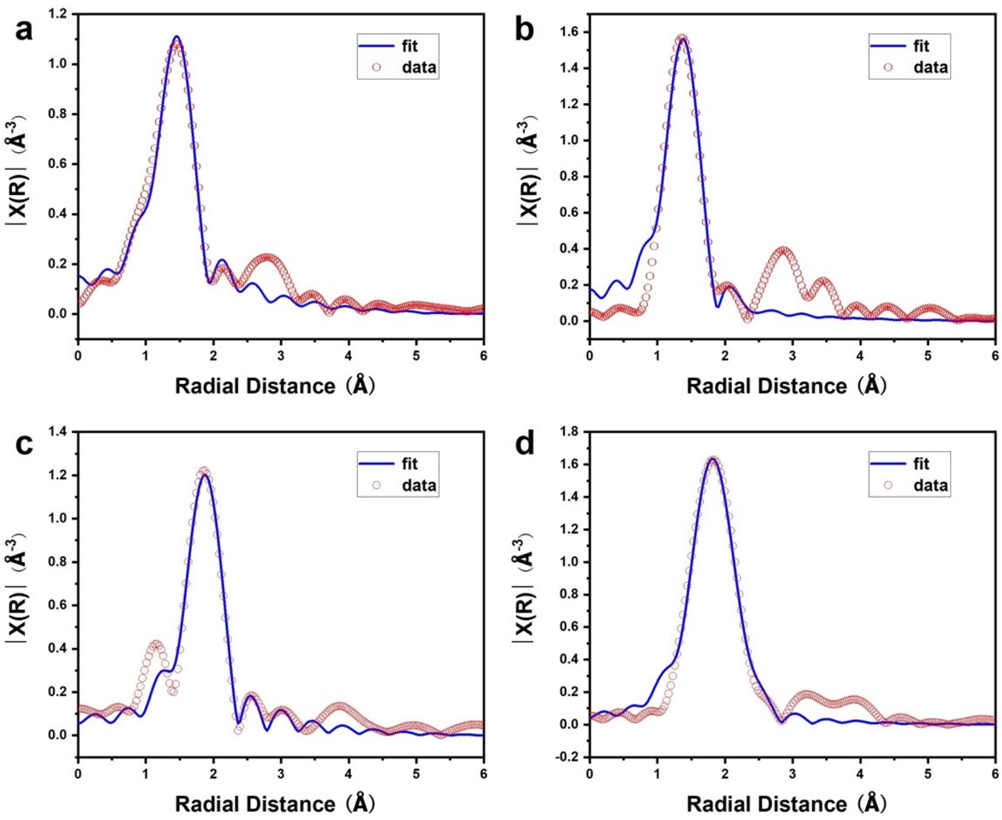


**Figure S10.** Ru K-edge EXAFS (points) and fit (line) for Ru powder (a), $RuO_2$ (b), $RuS_2$ (c) and $Ru_2(S_3Se)$ (d), shown in $k^2$ weighted $R$-space.

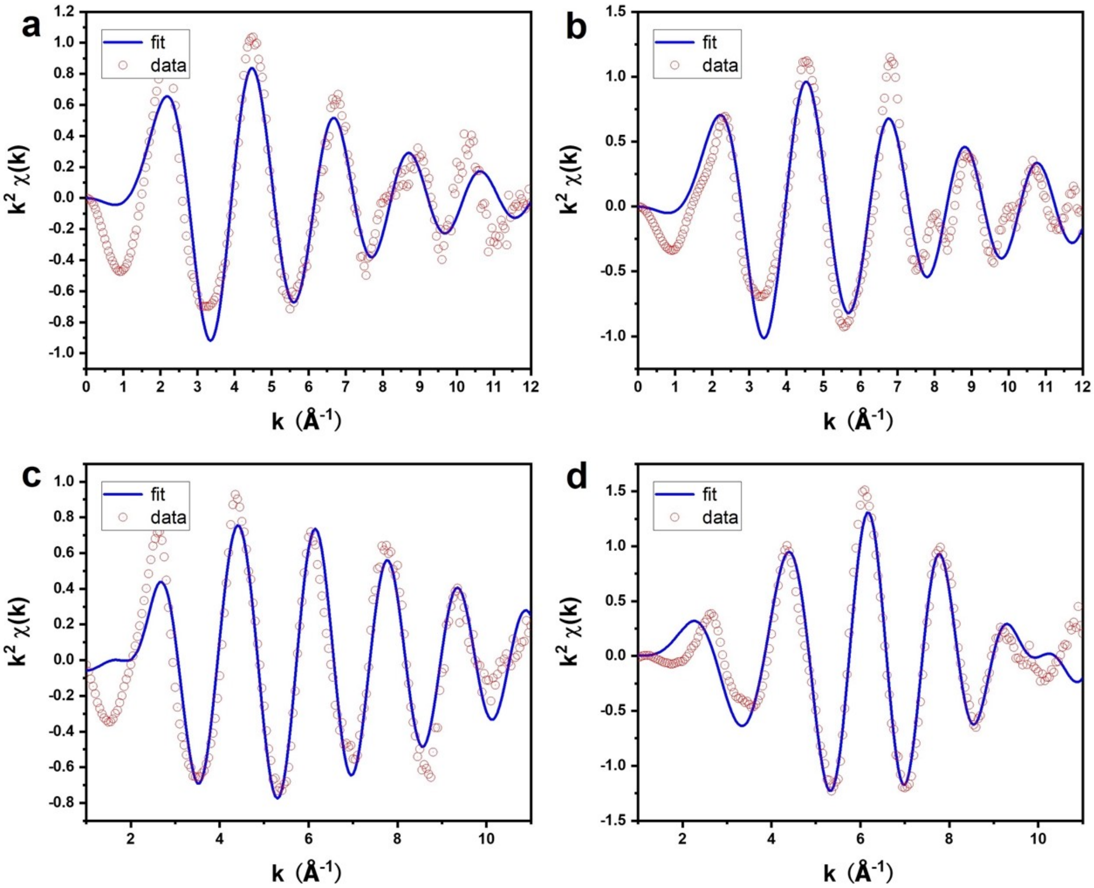


**Figure S11.** Ru K-edge EXAFS (points) and fit (line) for Ru powder (a), $RuO_2$ (b), $RuS_2$ (c) and $Ru_2(S_3Se)$ (d), shown in $k^2$ weighted *k*-space.

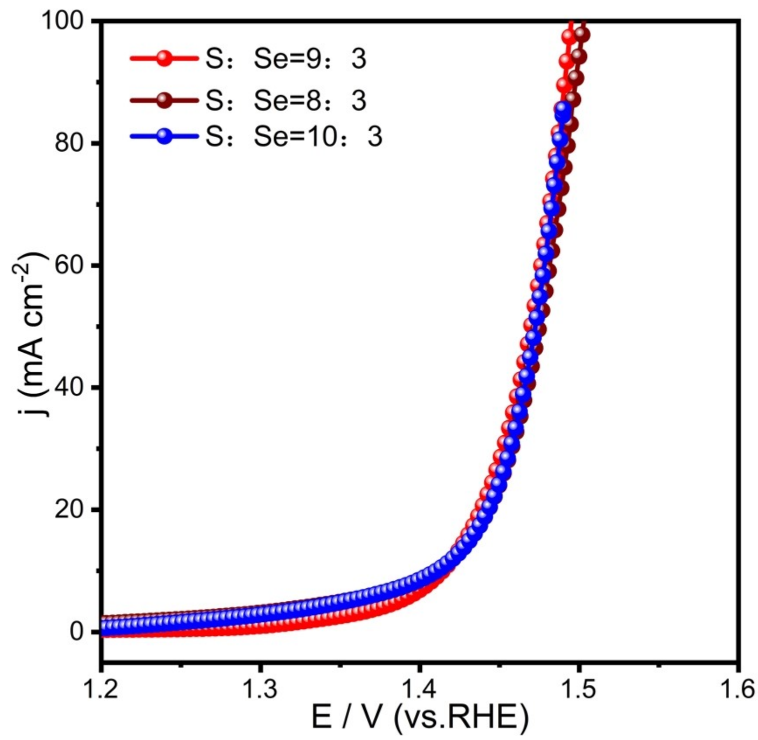


**Figure S12.** OER polarization curves of synthesized samples with different S/Se ratio.

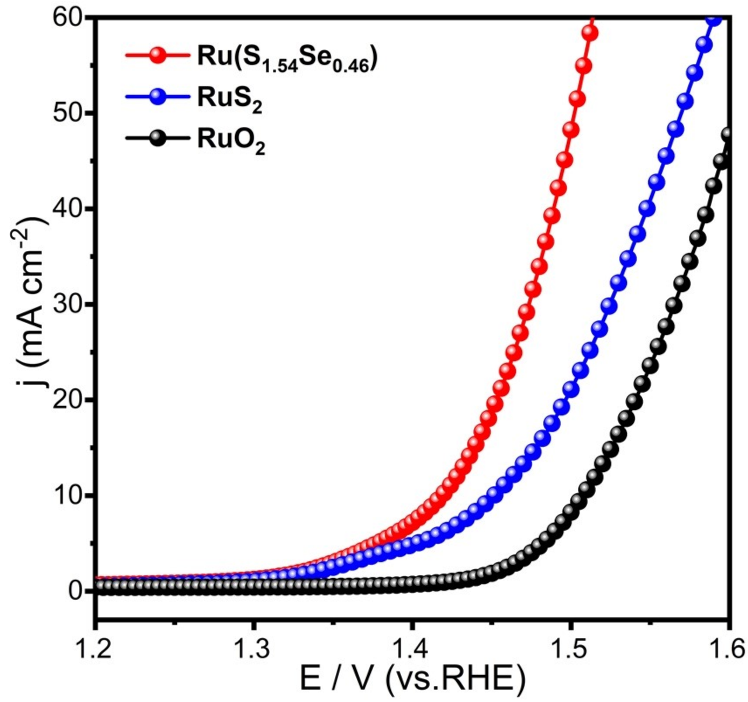


**Figure S13.** OER polarization curves without IR correction for $Ru_2(S_3Se)$, $RuS_2$ and commercial $RuO_2$.

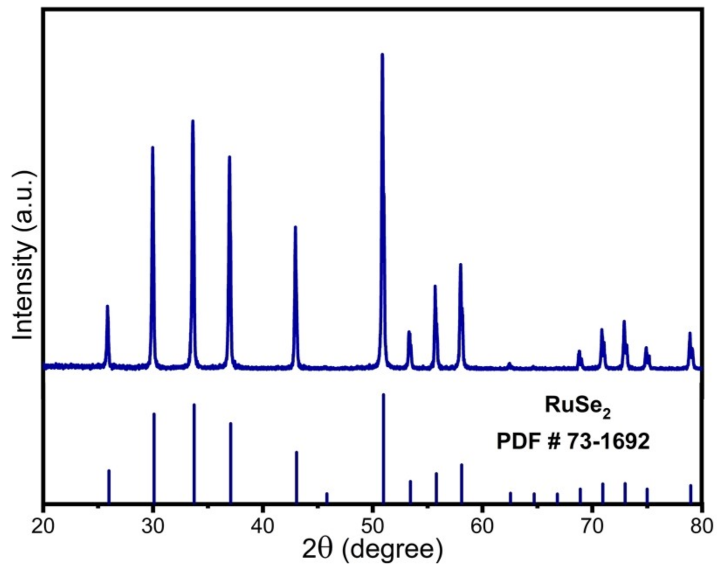


**Figure S14.** X-ray diffraction pattern of synthesized $RuSe_2$.

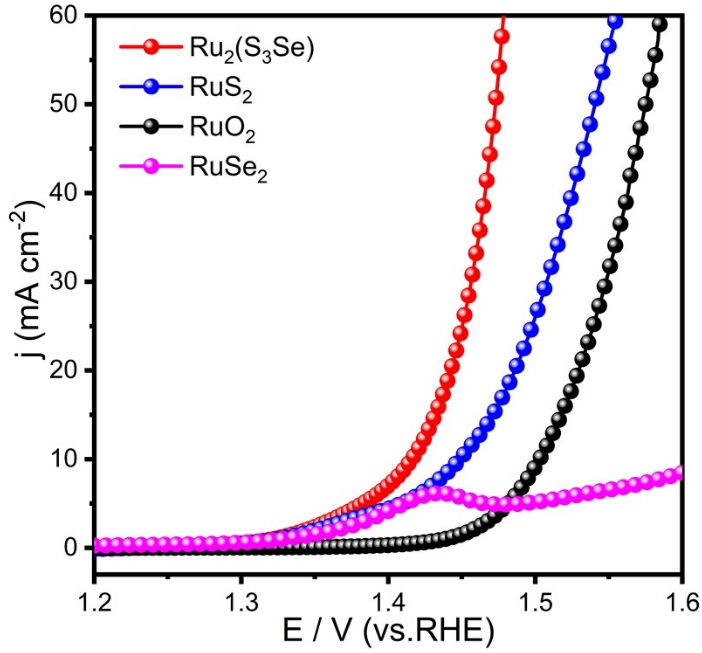


**Figure S15.** OER polarization curves of $Ru_2(S_3Se)$, $RuS_2$, $RuO_2$ and $RuSe_2$ in 0.5 M $H_2SO_4$.

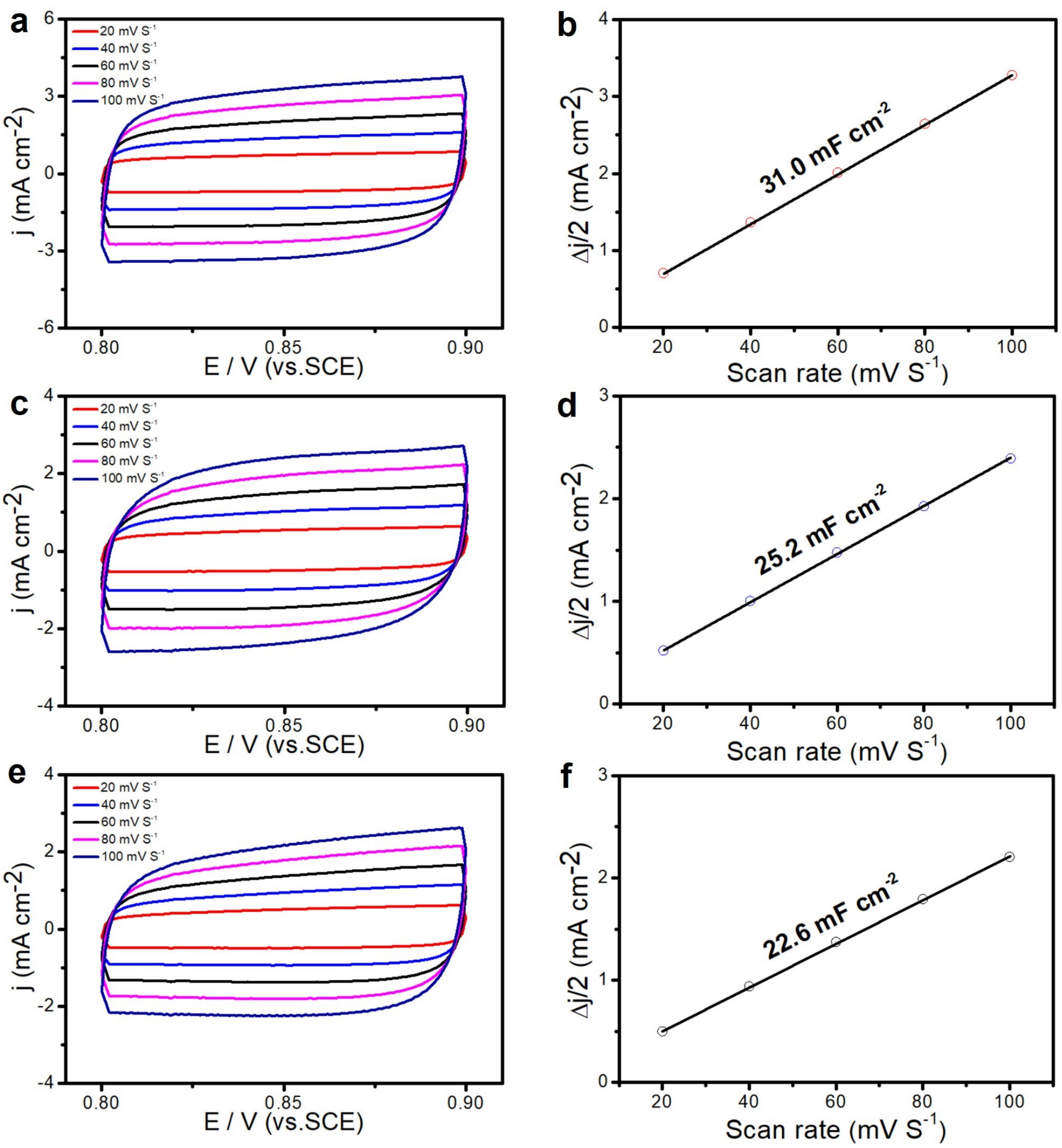


**Figure S16.** Cyclic voltammograms of (a) $Ru_2(S_3Se)$, (c) $RuS_2$ and (e) $RuO_2$ in the region of (0.80) - (0.90) V versus SCE at different scan rates. Corresponding linear relationships between capacitive current and scan rate of (b) $Ru_2(S_3Se)$, (d) $RuS_2$ and (f) $RuO_2$.

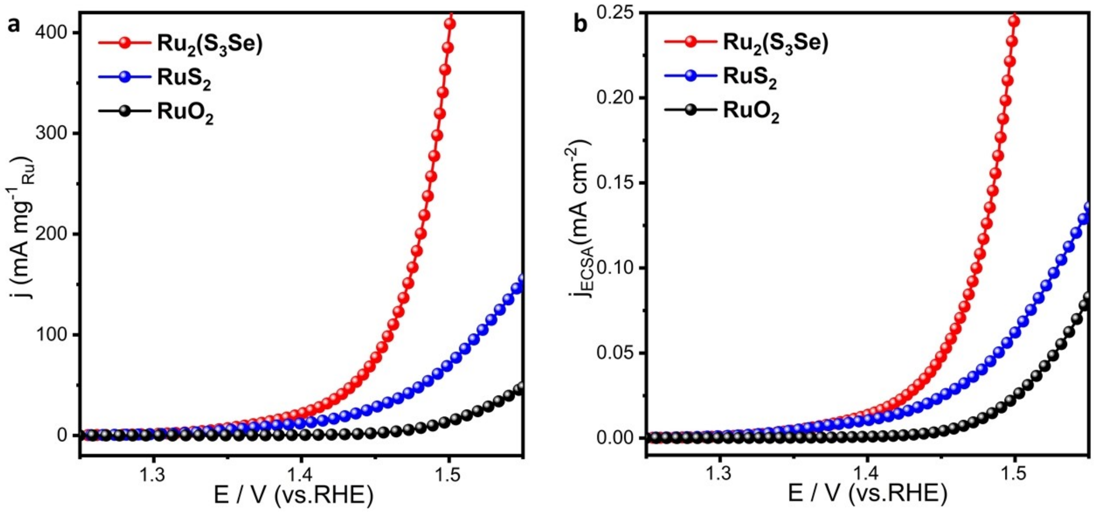


**Figure S17.** LSVs normalized by (a) Ru load and (b) ECSA value for OER in 0.5 M $H_2SO_4$.

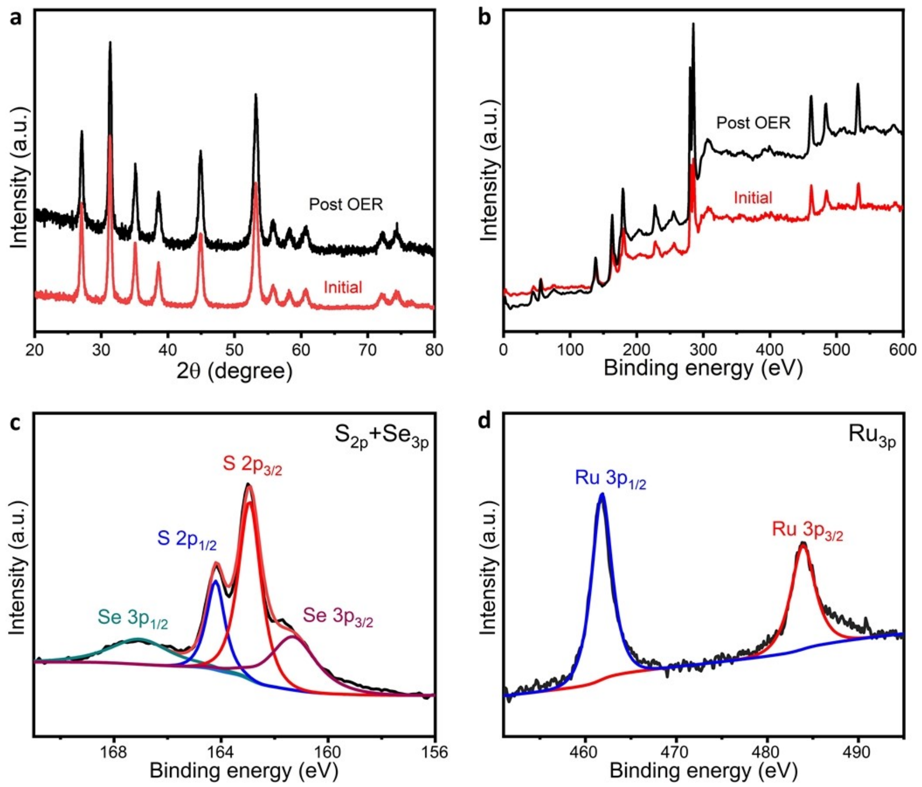


**Figure S18.** (a) XRD pattern and (b) XPS survey of $Ru_2(S_3Se)$ before and after OER electrolysis in 0.5 M $H_2SO_4$. (c) S 2p and Se 3p XPS spectrum of $Ru_2(S_3Se)$ after OER electrolysis. (d) Ru 3p XPS spectrum of $Ru_2(S_3Se)$ after OER electrolysis.

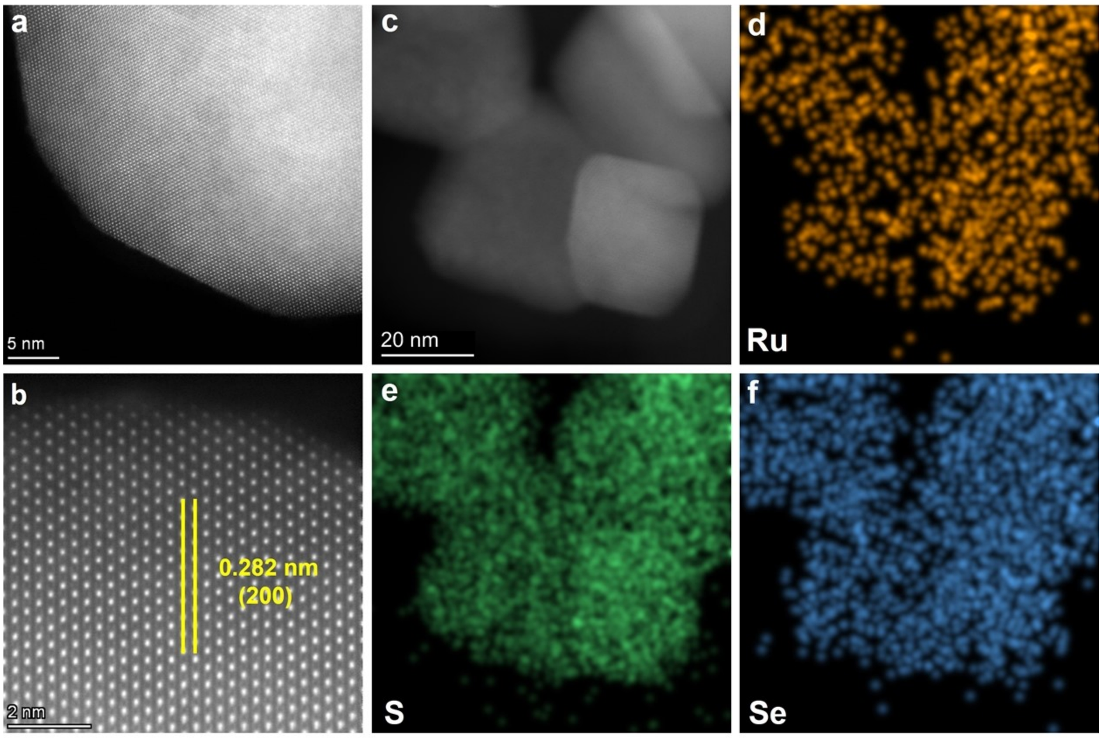


**Figure S19.** (a, b) STEM images of $Ru_2(S_3Se)$ after OER electrolysis in 0.5 M $H_2SO_4$. (c-f) HAADF-STEM image and corresponding EDS elemental maps for Ru, S and Se.

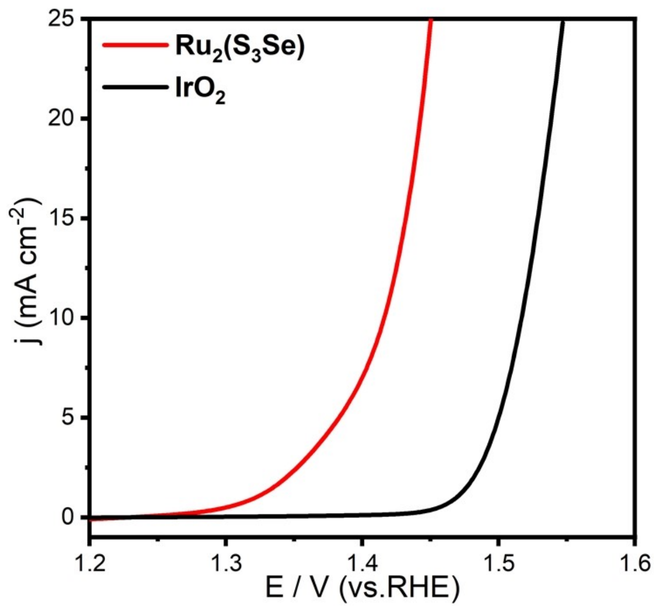


**Figure S20.** OER polarization curves of $Ru_2(S_3Se)$ and commercial $IrO_2$ in 0.5 M $H_2SO_4$.

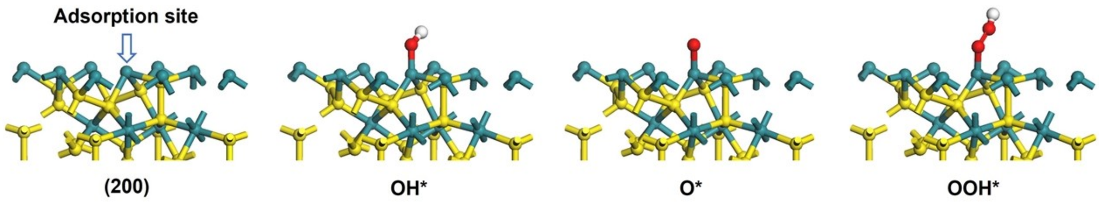


**Figure S21.** The four-step OER process at the adsorption site of $RuS_2$.

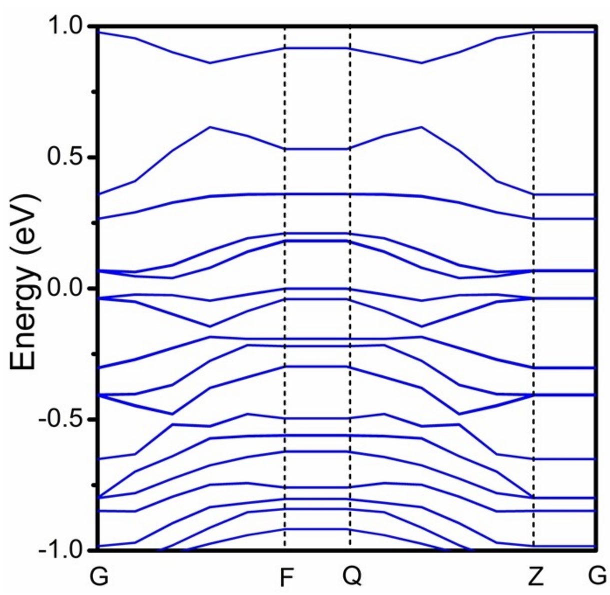


**Figure S22.** The band structures of $RuS_2$.

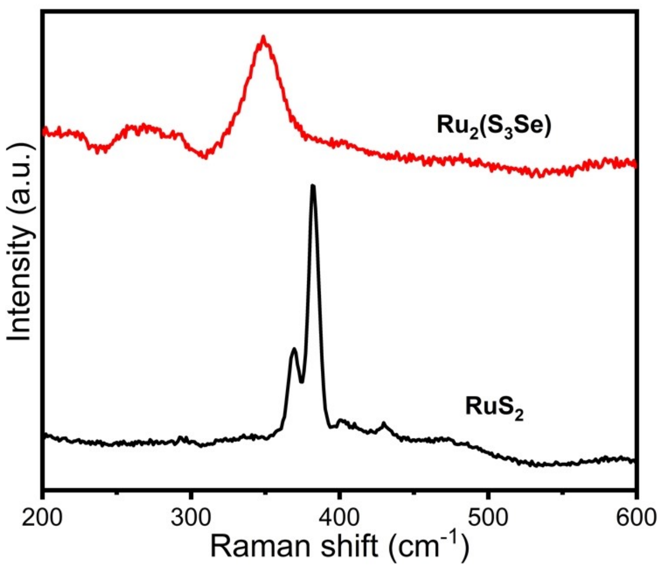


**Figure S23.** Raman spectra of $RuS_2$ and $Ru_2(S_3Se)$ mensurated under dry conditions.

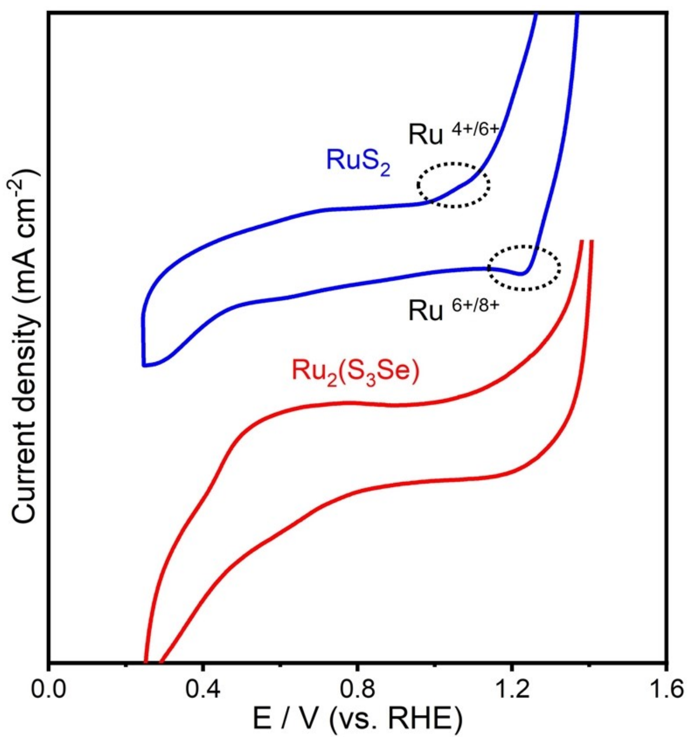


**Figure S24.** CV analysis of redox peak of $RuS_2$ and $Ru_2(S_3Se)$ measured from 0.0 to 1.2 V vs. SCE.

**Table S1.** Comparison of OER performance of $Ru_2(S_3Se)$ with recently reported Ru/Ir-based electrocatalysts at 10 mA $cm^{-2}$ in acidic media.

| Catalyst | Electrolyte | η (mV) at 10 mA $cm^{-2}$ (mass loading) | reference |
|---|---|---|---|
| $Ru_2(S_3Se)$ | 0.5 M $H_2SO_4$ | 186 (0.32 mg $cm^{-2}$) | This work |
| RuIr@CoNC | 0.5 M $H_2SO_4$ | 223 (50 μg $cm^{-2}$) | [1] |
| Ir-CCTO | 0.5 M $H_2SO_4$ | 280 (0.35 mg $cm^{-2}$) | [2] |
| $Ru_1Ir_1O_x$ | 0.5 M $H_2SO_4$ | 204 (0.15 mg $cm^{-2}$) | [3] |
| $RuO_2$ /$(Co,Mn)_3O_4$ | 0.5 M $H_2SO_4$ | 270 (-) | [4] |
| SrRuIr | 0.5 M $H_2SO_4$ | 190 (0.32 mg $cm^{-2}$) | [5] |
| $Ir/Nb_2O_{5-x}$ | 0.5 M $H_2SO_4$ | 218 (-) | [6] |
| RuCu NSs | 0.5 M $H_2SO_4$ | 260 (-) | [7] |
| Rh-$RuO_2$ | 0.5 M $H_2SO_4$ | 239 (0.45 mg $cm^{-2}$) | [8] |
| Ru/$RuS_2$ | 0.5 M $H_2SO_4$ | 201 (0.85 mg $cm^{-2}$) | [9] |
| $RuB_2$ | 0.5 M $H_2SO_4$ | 223 (0.26 mg $cm^{-2}$) | [10] |
| $Cr_{0.6}Ru_{0.4}O_2$ | 0.5 M $H_2SO_4$ | 178 (0.29 mg $cm^{-2}$) | [11] |
| $CaCu_3Ru_4O_{12}$ | 0.5 M $H_2SO_4$ | 171 (0.25 mg $cm^{-2}$) | [12] |
| $RuO_2$ NSs | 0.5 M $H_2SO_4$ | 199 (125 μg $cm^{-2}$) | [13] |
| $W_{0.57}Ir_{0.43}O_{3-\delta}$ | 1 M $H_2SO_4$ | 370 (0.84 mg $cm^{-2}$) | [14] |
| a-$RuTe_2$ PNRs | 0.5 M $H_2SO_4$ | 242 (0.20 mg $cm^{-2}$) | [15] |
| $Nb_{0.1}Ru_{0.9}O_2$ | 0.5 M $H_2SO_4$ | 204 (0.51 mg $cm^{-2}$) | [16] |
| Ti-$IrO_x$/Ir | 0.5 M $H_2SO_4$ | 254 (-) | [17] |
| Ru@$IrO_x$ | 0.05 M $H_2SO_4$ | 282 (0.05 mg $cm^{-2}$) | [18] |
| IrW-$W_2B$ | 0.5 M $H_2SO_4$ | 291 (0.25 mg $cm^{-2}$) | [19] |
| Li-$IrO_x$ | 0.5 M $H_2SO_4$ | 300 (1 mg $cm^{-2}$) | [20] |
| $IrO_x$/$SrIrO_3$ | 0.5 M $H_2SO_4$ | 270 (-) | [21] |
| B-$RuO_2$ | 0.5 M $H_2SO_4$ | 200 (0.29 mg $cm^{-2}$) | [22] |
| Ir:$WO_3$/Ir | 0.5 M $H_2SO_4$ | 260 (-) | [23] |

## References:


1. Xu, J. et al. Atomic-Step Enriched Ruthenium–Iridium Nanocrystals Anchored Homogeneously on MOF-Derived Support for Efficient and Stable Oxygen Evolution in Acidic and Neutral Media. *ACS Catal.* **11**, 3402-3413 (2021).
2. Thao, N.T.T. et al. Colossal Dielectric Perovskites of Calcium Copper Titanate (CaCu3Ti4O12) with Low-Iridium Dopants Enables Ultrahigh Mass Activity for the Acidic Oxygen Evolution Reaction. *Adv. Sci.* **10**, 2207695 (2023)
3. He, J., Zhou, X., Xu, P. & Sun, J. Regulating Electron Redistribution of Intermetallic Iridium Oxide by Incorporating Ru for Efficient Acidic Water Oxidation. *Adv. Energy Mater.* **11**, 2102883 (2021).
4. Niu, S. et al. Low Ru loading RuO2/(Co,Mn)3O4 nanocomposite with modulated electronic structure for efficient oxygen evolution reaction in acid. *Appl. Catal., B* **297**, 120442 (2021).
5. Wen, Y. et al. Stabilizing Highly Active Ru Sites by Suppressing Lattice Oxygen Participation in Acidic Water Oxidation. *J. Am. Chem. Soc.* **143**, 6482-6490 (2021).
6. Shi, Z. et al. Enhanced Acidic Water Oxidation by Dynamic Migration of Oxygen Species at the Ir/Nb2O5−x Catalyst/Support Interfaces. *Angew. Chem., Int. Ed.* **61**, e202212341 (2022).
7. Yao, Q. et al. Channel-Rich RuCu Nanosheets for pH-Universal Overall Water Splitting Electrocatalysis. *Angew. Chem., Int. Ed.* **58**, 13983-13988 (2019).
8. Wang, Y. et al. Unraveling oxygen vacancy site mechanism of Rh-doped RuO2 catalyst for long-lasting acidic water oxidation. *Nat. Commun.* **14**, 1412 (2023).
9. Zhu, J. et al. Regulative Electronic States around Ruthenium/Ruthenium Disulphide Heterointerfaces for Efficient Water Splitting in Acidic Media. *Angew. Chem., Int. Ed.* **60**, 12328-12334 (2021).
10. Chen, D. et al. Ionothermal Route to Phase-Pure RuB2 Catalysts for Efficient Oxygen Evolution and Water Splitting in Acidic Media. *ACS Energy Letters* **5**, 2909-2915 (2020).
11. Lin, Y. et al. Chromium-ruthenium oxide solid solution electrocatalyst for highly efficient oxygen evolution reaction in acidic media. *Nat. Commun.* **10**, 162 (2019).
12. Miao, X. et al. Quadruple perovskite ruthenate as a highly efficient catalyst for acidic water oxidation. *Nat. Commun.* **10**, 3809 (2019).
13. Zhao, Z.L. et al. Boosting the oxygen evolution reaction using defect-rich ultra-thin ruthenium

oxide nanosheets in acidic media. *Energy Environ. Sci.* **13**, 5143-5151 (2020).

14. Kumari, S. et al. A low-noble-metal W1−xIrxO3−δ water oxidation electrocatalyst for acidic media via rapid plasma synthesis. *Energy Environ. Sci.* **10**, 2432-2440 (2017).

15. Wang, J. et al. Amorphization activated ruthenium-tellurium nanorods for efficient water splitting. *Nat. Commun.* **10**, 5692 (2019).

16. Liu, H. et al. Eliminating over-oxidation of ruthenium oxides by niobium for highly stable electrocatalytic oxygen evolution in acidic media. *Joule* **7**, 558-573 (2023).

17. Wang, Y. et al. Inverse doping IrOx/Ti with weakened Ir-O interaction toward stable and efficient acidic oxygen evolution. *Chem* **9**, 2931-2942 (2023).

18. Shan, J. et al. Charge-Redistribution-Enhanced Nanocrystalline Ru@IrOx Electrocatalysts for Oxygen Evolution in Acidic Media. *Chem* **5**, 445-459 (2019).

19. Li, R. et al. IrW nanochannel support enabling ultrastable electrocatalytic oxygen evolution at 2 A cm-2 in acidic media. *Nat. Commun.* **12**, 3540 (2021).

20. Gao, J. et al. Breaking Long-Range Order in Iridium Oxide by Alkali Ion for Efficient Water Oxidation. *J. Am. Chem. Soc.* **141**, 3014-3023 (2019).

21. Seitz, L.C. et al. A highly active and stable IrOx/SrIrO3 catalyst for the oxygen evolution reaction. *Science* **353**, 1011-1014 (2016).

22. Liu, C. et al. Motivating Ru-bri site of RuO2 by boron doping toward high performance acidic and neutral oxygen evolution. *Nano Research* **15**, 7008-7015 (2022).

23. Shi, X. et al. Efficient and Stable Acidic Water Oxidation Enabled by Low-Concentration, High-Valence Iridium Sites. *ACS Energy Letters* 7, 2228-2235 (2022).